On modeling the potential impacts of CO_2 sequestration on shallow groundwater: transport of organics and co-injected H_2S by supercritical CO_2 to shallow aquifers.

[1]*Liange Zheng, [1]Nicolas Spycher, [1]Jens Birkholzer, [1]Tianfu Xu, [1]John Apps and [2]Yousif Kharaka

[1]Lawrence Berkeley National Laboratory, Berkeley, CA 94720, USA

[2] U.S Geological Survey, Menlo Park, CA 94205, USA

* corresponding author, e-mail: lzheng@lbl.gov

Abstract

Proper site selection for CO_2 geologic storage requires assessing the impact of potential leakage of CO_2 from deep subsurface reservoirs to overlying drinking water aquifers. Although recent studies have largely focused on the mobilization of trace elements in response to the intrusion of CO_2 into such aquifers, in this paper we investigate two other leakage issues and potential effects on groundwater quality: the transport of organic compounds by supercritical CO_2 from deep storage reservoirs and the upward migration of CO_2 with co-injected H_2S. Numerical simulations show that organic compounds that may be present at depth, such as benzene, could be mobilized by supercritical CO_2 and migrate with the leaking CO_2. Modeling results also show that upon the transport of

CO_2+H_2S mixtures through a hypothetical leakage pathway, H_2S arrival in the shallower aquifer is delayed in comparison with that of CO_2 due to the preferential dissolution of H_2S into the aqueous phase. The potentially adverse impacts of leakage on shallow groundwater quality may be exacerbated for cases of leaking CO_2+H_2S, compared to intrusion of pure CO_2, possibly leading to the mobilization of thiophilic elements such as arsenic. Geochemical reactions included in the simulations involve adsorption/desorption, reductive dissolution of goethite, precipitation of pyrite, siderite, and arsenic sulfide phases. The models presented are generic in nature, exploring important processes regarding organic compounds and co-injected H_2S, and calling attention to the need for more site-specific studies taking into account the variability and uncertainty of key hydrogeologic and geochemical parameters.

1. Introduction

CO_2 capture and geologic storage is being considered as a potential mitigation measure to rising anthropogenic emissions of greenhouse gases. The feasibility of geologic storage requires not only the assessment of deep reservoir integrity, but also must consider the impact of potential CO_2 leakage from deep subsurface reservoirs on overlying groundwater aquifers to ensure the safety of drinking water resources at these locations. The leakage of CO_2 could affect overlying potable aquifers in several ways. First, the dissolution of CO_2 in water increases the concentration of dissolved carbonic acid and thus increases acidity, which could mobilize trace elements through mineral dissolution, desorption reactions, and/or exchange reactions involving H^+ and other mobilized

constituents (e.g., Aiuppa et al., 2005; Zheng et al., 2009; Kharaka et al., 2010; Little and Jackson, 2010; Wilkin and Digiulio, 2010; Zheng et al., 2012; Trautz et al., 2012). In addition, the increased dissolved CO_2 concentrations could result in desorption of metals such as arsenic by competitive sorption of carbonate ions (Appelo et al., 2002). Second, because supercritical CO_2 (SCC) is also an excellent solvent for organic compounds (Anitescu and Tavlarides, 2006; Kharaka et al., 2009), concerns have been raised about the potential mobilization of organic constituents from depth and subsequent transport to shallow drinking water bodies via leakage pathways. Third, the co-injection of H_2S in geologic sequestration operations is being considered because the burning of fossil fuels can emit significant amounts of H_2S and SO_2 (which disproportionates into H_2S and H_2SO_4) in addition to CO_2. Because the separation of these gas impurities from power plant effluents is quite costly, and their release to the atmosphere is environmentally harmful, it may be advantageous to consider co-injecting these gases. If the co-injection of H_2S is deployed, the impact of CO_2+H_2S leakage from deep saline reservoirs to overlying shallow aquifers is also a question that the scientific community must answer for the public.

Recently, the potential mobilization of trace elements in response to CO_2 intrusion into potable groundwater has been investigated by laboratory experiments (McGrath et al., 2007; Smyth et al., 2009; Lu et al., 2010; Little and Jackson, 2010), natural analogues (e.g., Aiuppa et al. 2005; Flaathen et al. 2009; Keating et al., 2010; Arnorsson et al., 2010), field experiments (Kharaka et al., 2010; Trautz et al., 2012) and numerical models (Wang and Jaffe, 2004; Carroll et al., 2009; Zheng et al., 2009; Apps et al., 2010; Wilkin

and Digiulio, 2010, Zheng et al., 2012). These studies helped for the understanding of the risk brought by CO_2 itself. However, once leakage accurs, the CO_2-rich phase could contains impurites such organics and co-injected H_2S that jeoperdize groundwtater as well. To the best of our knowledge, little work has been conducted with respect to potential impact on groundwater from organic constituents and co-injectants such as H_2S. For example, while the possible extraction of organic compounds by supercritical CO_2 inside deep reservoirs is a well-known phenomenon (e.g., Kharaka and Hanor, 2007), the potential for groundwater contamination from mobilized organic constituents transported to shallow aquifers has not been studied, to our knowledge. Kharaka et al. (2009) advocated further investigation of this issue when elevated DOC concentrations were observed in the injection formation at the Frio test site in Texas. The effect of co-injected H_2S on mineral trapping of CO_2 and mineralogical alteration of reservoir host rocks has been investigated previously (Gunter et al., 2000; 2005; Knauss et al., 2005; Palandri and Kharaka, 2005; Palandri et al., 2005; Xu et al., 2007; Murphy et al., 2010; 2011, Lammers et al., 2011), but with focus on the geochemical evolution in the storage formation at relatively high temperature and pressure ($T>70^oC$, $P>150$ bar). The behavior of co-injected H_2S along a leakage pathway has been shown to be affected by chromatographic partitioning between CO_2 and water (Bachu and Bennion, 2009; Bachu et al., 2009). However the potential consequences of CO_2+H_2S mixtures intruding into a shallow groundwater aquifer have remained largely uninvestigated.

In this paper, we evaluate the aforementioned issues related to organic compounds and co-injected H_2S by means of three exploratory numerical simulations. The first model

considers a storage formation, an overlying aquifer, and a leakage pathway between them, to simulate a hypothetical scenario in which trace benzene in deep formations is mobilized by CO_2 injection, then transported vertically along a preferential pathway into an overlying shallow aquifer. The second model is setup in a similar fashion as the first one, but was developed to study the fate of H_2S in the storage formation and its behavior along a potential leakage pathway. The third model builds on a study by Zheng et al. (2009). The intrusion of CO_2+H_2S mixtures into a shallow fresh water aquifer is simulated to examine the interaction of CO_2+H_2S with metal-bearing sediments in the aquifer.

The objective of this paper is to bring attention to potential reactive processes accompanying the migration of CO_2 from a deep storage reservoir to overlying shallow dilute water aquifers, and to illustrate these processes using rather simplified numerical models that should be regarded as more qualitative than quantitative. Our goal is not to make predictions for any particular storage sites, but to point to the need for more site-specific studies regarding potential co-migration of organic compounds and H_2S with CO_2 from deep storage reservoirs, and resulting impact to overlying drinking water aquifers. We start with a brief introduction of the simulation tool and then present the aforementioned three models separately, followed by some concluding remarks. Further details on this study can be found in an unpublished report conducted by the authors for the U.S. Environmental Protection Agency (Zheng et al., 2010).

2. Simulator --- *TMVOC_REACT*

The modeling work presented in this paper is conducted with TMVOC_REACT, a simulator that links TMVOC (Pruess and Battistelli, 2002) and TOUGHREACT (Xu et al., 2006). TOUGHREACT (Xu et al., 2006, 2011) is a numerical simulation program for chemically reactive nonisothermal flows of multiphase fluids in porous and fractured media. The program was developed by introducing reactive chemistry into the multiphase fluid and heat flow simulator TOUGH2 (Pruess et al., 1999). A variety of subsurface thermo-physical-chemical-biological processes are considered under a wide range of hydrological and geochemical conditions.. In TMVOC_REACT, the fluid and heat flow simulator in TOUGHREACT was replaced with TMVOC (Pruess and Battistelli, 2002), a numerical simulator for three-phase nonisothermal flow of multicomponent hydrocarbon mixtures in variably saturated heterogeneous media.

TMVOC was initially designed for studying subsurface contamination by volatile organic compounds (VOCs), such as hydrocarbon fuels and industrial solvents. In the TMVOC formulation, the multiphase system is assumed to be composed of water, noncondensable gases (NCGs), and water-soluble volatile organic chemicals (VOCs). The number and nature of NCGs and VOCs can be specified by the user. NCGs currently available include O_2, N_2, CO_2, CH_4, ethane, ethylene, acetylene, and air (a pseudo-component treated with properties averaged from N_2 and O_2). Thermophysical property data for VOCs must be provided by the user. The fluid components may partition (volatilize and/or dissolve) among gaseous, aqueous, and NAPL phases. Any combination of the three phases may be present, and phases may appear and disappear in the course of a simulation.

In TMVOC_REACT, gas partial pressures and fugacity coefficients computed from the flow module (TMVOC) are passed to the geochemical module (-REACT) for calculating dissolved concentrations in water. The routine GASEOS (Reagan and Oldenburg, 2006; Moridis et al., 2008) was incorporated into TMVOC_REACT for computation of multi-component gas mixture properties, including new parameters and formulations for the phase partitioning of benzene and H_2S in addition to CO_2, as discussed later. The GASEOS routine incorporates several standard cubic equations of state such as Redlich-Kwong (RK), Peng-Robinson (PR), and Soave-Redlich-Kwong (SRK) (e.g., Orbey and Sandler, 1998). Consumption or production of components from the solid phase is coupled back to fluid flow, but lagging one time step to avoid time-consuming computation of partial derivatives (explicit coupling). This approach preserves the accuracy of mass balances and is accurate enough for most simulated problems. Changes in porosity and permeability due to mineral dissolution/precipitation computed by the chemical module are fed back to the flow module for next-time-step calculations.

3. Transport of organic compounds in a hypothetical leakage scenario

The solvent properties of SCC for organic compounds have long been recognized and are one of the reasons CO_2 flooding of hydrocarbon reservoirs has been practiced for years to enhance oil recovery (e.g., Bondor, 1992). SCC has also been lauded as an environmentally friendly solvent, and its use to decontaminate soils impacted by hazardous organic compounds is regarded as a "green" cleanup technology (e.g., Anitescu and Tavlarides, 2006; Green and Akgerman, 1996; Hauthal, 2001; Smyth et al.,

1999) because it avoids the use of other more hazardous solvents. Given these considerations, there are good reasons to evaluate the potential for mobilization of organics from deep storage reservoirs to overlying freshwater aquifers upon leakage from CCS operations. TMVOC_REACT was used to assess the potential for SCC (1) to mobilize and transport organic compounds in deep geologic formations (using benzene as an example) and (2) to possibly contaminate potable groundwater if leakage occurred from depth into an overlying fresh water aquifer.

3.1. Conceptual Mobilization Scenario

The scenario considered in our modeling study is that of SCC being injected into a deep saline aquifer. Because SCC is less dense than water, some SCC migration is expected upward along the dip of the storage formation, up to a point where the SCC plume would become immobilized by a structural trap (e.g., low-permeability/porosity cap rock) and/or by capillary trapping as the SCC saturation decreases below the threshold residual saturation (e.g., Doughty and Pruess, 2005; Silin et al., 2009). Because SCC is a well-known solvent for organics (e.g., Anitescu and Talvarides 2006), it is expected to dissolve organic compounds present in the storage formation and to transport these compounds within the confined CO_2 reservoir. The main question being evaluated here is the extent of such transport, within the reservoir and in the event of leakage from the reservoir to shallower formations, for example through fault or fracture zones, or poorly plugged abandoned wells.

Solid-aqueous-SCC phase partitioning data is needed for each organic compound considered in the simulations. Because these data are lacking or highly uncertain for many compounds of potential interest, our study focused on benzene as a "proxy" compound, on the basis of the following considerations. Organic compounds present in deep saline aquifers are seldom reported. However, their occurrence and concentrations in brines produced in the vicinity of gas and oil fields have been documented (e.g., RøeUtvik, 1999; Witter and Jones, 1999). From such studies, benzene, toluene, ethylbenzene, and xylenes (BTEX), polycyclic aromatic hydrocarbons (PAHs) and phenols were identified as potentially relevant candidates for our study. Obviously, many other organics could also warrant attention. Such compounds include carboxylic acids, which are commonly present at much higher concentrations (up to 5,000 mg/L) in oil field brines (Kharaka and Hanor, 2007) and are also expected in deep saline aquifers. Although these compounds are essentially nontoxic, they are good ligands for metal complexation, and their mobilization could exacerbate the release of trace metals upon SCC leakage into fresh water. Benzene was eventually selected for further investigation in this study because of: (1) its relatively low U.S. EPA Maximum Contaminant Level (similar to phenol but higher than PAH), (2) its high solubility in SCC (3-5 times higher than phenol and 2-5 orders of magnitude higher than PAHs), (3) its relatively high solubility in water (lower than phenol but higher than PAHs), and (4) its high partition coefficient between SCC and water (e.g. Ghonasgi et al., 1991).

McAuliffe (1969) reported the dissolved hydrocarbon content of typical subsurface brines recovered by conventional drill-stem tests in exploratory wells, revealing a wide range of

values, from 0.86×10^{-3} to 8.65 mg/L. A study by Zarrella et al. (1967) provides additional data on benzene concentrations in oil field brines, ranging from undetectable to 18.6 mg/L. These authors investigated the concentration of benzene in formation brines from development and wildcat wells at various distances from petroleum reservoirs and at various depths, covering barren and producing horizons. Their study shows that benzene concentrations decrease away from reservoirs, and away from producing horizons. These authors also observed that brine from a unit separated by only 90 ft of shale from an oil pool contained only traces (less than 0.02 ppm) of benzene. Sirivedhin and Dallbauman (2004) made similar observations in a study of benzene concentrations from the Osage-Skiatook Petroleum Environmental Research site, Osage County, Oklahoma. In their study, the maximum concentration of benzene in produced water was found to be 0.53 mg/L, whereas the concentration of benzene in groundwater above the production zone was only 0.001 mg/L. Based on these investigations, and the fact that our modeling study considers CO_2 injection into a deep saline formation that is not necessarily in the vicinity of an oil reservoir, an initial benzene concentration of 0.001 mg/L is assumed in the targeted deep saline aquifer. Note that this value is 5 times smaller than the EPA-regulated Maximum Contaminant Level for benzene (0.005 mg/L, 5 ppb) in drinking water.

Other important parameters constraining the total amount of benzene that could be leached from a deep saline aquifer are (1) the amount of organic matter in the sediments, and (2) the amount of benzene associated with the organic matter. Kraemer and Reid (1984) mentioned that the bulk of organic matter amount in Gulf Coast sediments is

contained within shale and is generally small (0.31–1.0 wt.% total organic carbon). Organic matter concentrations in sandstones are typically much lower. In the current study, we conservatively assume that the deep saline aquifer is an impure sandstone containing 1.0 wt.% of organic matter as a generic "kerogen" phase. The amount of benzene in the kerogen is arbitrarily assumed to be 0.01 ppm, which corresponds to 1×10^{-4} ppm benzene in the sediment. The kerogen phase is treated in the model like a mineral, with a negligible dissolution rate given the short simulated time frames considered here (e.g., Freund and Kelemen, 1989), but the capacity to retain benzene via sorption. The following generalized surface complexation reaction is used to express the distribution of benzene between the aqueous and solid (kerogen) phases:

$$SOH\text{-}C_6H_6 = SOH + C_6H_6(aq) \qquad \log K_{scm} = -1.9$$

Where $SOH\text{-}C_6H_6$ represent a generalized sorbed benzene phase on the surface of kerogen, $C_6H_6(aq)$ is aqueous benzene, SOH is the concentration of unoccupied sorption sites, all in units of mol/kg_{water}. Details on how K_{scm} was calculated are given in Appendix A. The phase partitioning of benzene in SCC and water is computed from the GASEOS routine of TMVOC_REACT, using a modified Soave Redlich-Kwong (SRK) equation of state with parameters from Reid et al. (1986).

3.2. Model setup

Our modeling study uses a relatively simple conceptual setup intended for a more qualitative than quantitative purpose. Benzene is leached by SCC in a deep storage

formation and is subsequently transported by SCC along a vertical leakage pathway to a shallow aquifer. No solid-phase partitioning (sorption) is assumed to take place along the leakage pathway or in the shallow aquifer, thus maximizing aqueous benzene concentrations. The pressure and temperature path followed along the vertical pathway are controlled by hydrostatic pressure and a typical geothermal gradient (30^{o}C/1000 m). It should be noted that TMVOC_REACT currently does not allow "flashing" from supercritical or liquid CO_2 to gaseous CO_2 conditions. For this reason, pressure and temperature, although decreasing along the leakage pathway, are kept within the supercritical or liquid domain.

Figure 1 shows a schematic representation of the model setup including initial and boundary conditions. The 2-D cross section includes a deep storage formation, an overlying aquifer, and a leakage pathway that connects the two aquifers. The leakage pathway is simulated as a zone of high permeability. Aquitards are included in the model between the storage formation and the overlying aquifer, as well as above this aquifer. Pressures on the left and right (vertical) boundaries are fixed. A 1/100 gradient is imposed on the flow field with a regional gradient direction from left to right. CO_2 is injected at a rate of 0.1 kg/s (~3.2 kt/y) in a well which is located 200 m from the left model boundary and is perforated through the entire storage formation (with the well simulated as a stack of model gridblocks). The bottom of the vertical leakage pathway is located 100 m downgradient of the injection point (300 m from the left model boundary). Hydrostatic pressure conditions are assumed initially. The pressure at the top of the model domain is around 20 bar and that at the bottom is about 200 bar. Temperature is

fixed to 21°C at the top and 75°C at the bottom of the modeled domain. Table 1 lists the hydrogeological properties for the model. The leakage pathway is 6 m in width, and has the same properties as the storage formation, except for its permeability, which is one order of magnitude higher. The model domain is discretized with rectangle grid having uniform 10 m interval in the vertical direction. In the horizontal direction, the interval is 1 m inside the leakage pathway and then becomes larger and larger when approaching the left and right boundary with a maximum of 20 m.

The simulated time period is 3.5 years. At this point in time, the injected CO_2 in the storage formation has migrated into the fracture zone, moved upwards due to buoyancy forces and the vertical pressure gradient, and spread out laterally within the overlying aquifer, almost reaching the left boundary of the model domain. As discussed above, the initial benzene concentration in the aqueous phase is assumed to be ~ 1 μg/L in the storage formation (1.28×10^{-8} mol/kg_{water}), and is set arbitrarily four orders of magnitude lower in areas outside the storage formation (to 0.0001 μg/L). Solid-phase (sorbed) benzene is assumed present only within the storage formation, and at a concentration of 0.1 ppb in the sediments (1 wt% kerogen containing 0.01 ppm benzene).

3.3. Model results

The computed spatial distribution of SCC ("liquid") saturation is shown in Figure 2. The injected CO_2 is predicted to accumulate at the top of the storage formation and then move horizontally both up- and downgradient. When CO_2 encounters the fracture, it migrates

upward and eventually enters the overlying aquifer. The pressure buildup changes the flow field in the overlying aquifer and consequently CO_2 spreads laterally in both directions, towards the left and right boundaries.

The computed spatial distribution of the benzene mass fraction in SCC is shown in Figure 3. Because of the preferential partitioning of benzene into SCC, benzene in the storage formation is leached by the SCC from the aqueous phase and from sorption sites on the solid phase (kerogen). Benzene is then carried with the migrating SCC to the overlying aquifer. Because the aqueous solubility of benzene in contact with SCC is lower than the aqueous solubility of CO_2, benzene is continuously enriched at the front of the SCC plume as it advances, thus with the tip of the plume showing the highest mass fraction of benzene.

As shown in Figure 4, benzene is depleted from the aqueous phase in the vicinity of the the CO_2 injection point in the storage formation, because it is stripped by SCC. It is then introduced into the overlying shallow aquifer by the intrusion of benzene-laden SCC. The resulting benzene concentrations in the shallow aquifer after 3.5 years are on the same order of magnitude as the initial concentrations in the storage formation, with values up to 4.2×10^{-8} molal (~ 0.003 mg/L). At later times and with further migration in the shallow aquifer, these levels are likely to decrease due to diffusive/dispersive mixing. The predicted level of benzene contamination in the shallow aquifer (maximum concentration) depends mostly on the amount of benzene carried by SCC, which depends on the amount of benzene present at depth and SCC migration rates. Note that re-sorption of benzene onto sediments (organic matter) along the leakage pathway and in the shallow aquifer is

not considered, and therefore the computed benzene concentrations in the shallower aquifer are likely overestimated.

The assessment of organic compound mobilization and transport by SCC in deep aquifers requires knowledge of the nature of phases associated with organics, as well as sediment sorption characteristics for these compounds. These properties are not only quite site specific, they are also mostly unknown. Therefore, these results should not be seen as actual predictions applying to any particular site, but more as an illustration that organic compounds such as benzene could be transported by SCC, should leakage occur, reaching levels in shallow aquifers that would be quite site specific.

4. Transport of Co-injected H_2S in a hypothetical leakage scenario

Laboratory work (Bachu and Bennion, 2009) has shown that gases contained in a CO_2 injection stream will chromatographically partition when in contact with the brine present in deep saline aquifers. As described in Bachu et al. (2009), chromatographic partitioning of various gases, when in contact with subsurface fluids, is not a new phenomenon. Actually, this phenomenon has been used extensively in the petroleum industry for inter-well tracer tests to determine the oil saturation and reservoir properties between injection and observation wells (e.g., Illiassov and Datta-Gupta, 2002; Tang, 2005), and also for the detection and estimation of nonaqueous phase liquids (NAPLs) present in the groundwater and in the vadose zone at contaminated sites (e.g. Deeds et al., 2000). Numerical models (Bachu et al., 2009) have shown that the preferential H_2S solubility in

brine compared to that of CO_2 has a dominant effect on the chromatographic partitioning of these two gases, resulting in H_2S being stripped off at the leading edge of the advancing front of the CO_2+H_2S supercritical mixture.

The experimental and modeling work conducted by Bachu and Bennion (2009) and Bachu et al. (2009) was for column-scale systems. In addition, their experiments and corresponding numerical models were conducted under isothermal conditions and did not specifically address depth-dependent changes in pressure and temperature along a leakage pathway (e.g., a fracture zone or a fault). Assuming a hydrostatic pressure gradient and a geothermal gradient of 30°C/1000 m, the difference between computed CO_2 and H_2S aqueous solubilities significantly narrows with decreasing depth (Figure 5). Therefore, the chromatographic separation effect observed by Bachu and Bannion (2009) is expected to decrease as the H_2S+CO_2 mixture ascends along a leakage pathway, which would quicken H_2S breakthough into a shallow aquifer. Given this observation, a hypothetical scenario of leakage along a preferential pathway (including declining pressures and temperatures along the flow path) was simulated to investigate how the breakthrough of H_2S may be delayed compared with that of CO_2. Ultimately, the modeling objective was to determine whether the preferential dissolution of H_2S (1) could retard the arrival of H_2S in a freshwater aquifer compared to the breakthrough of CO_2, and (2) might reduce the maximum concentrations of H_2S in the groundwater.

4.1. Model setup

The model used for studying H_2S fate is very similar to that used for benzene (Figure 1). The differences are that (1) benzene is not present in the model domain and (2) a CO_2+ H_2S mixture (95 and 5% by weight, respectively) is injected into the storage formation instead of pure CO_2. The injection rate is assumed to be 0.1 kg/s (3.2×10^3 tonnes/year). The hydrogeological properties chosen for the model are the same as for the previously discussed model (Table 1).

The key parameters are those affecting the phase partitioning of H_2S and CO_2, including the solubility of these gases in the aqueous phase at varying subsurface pressure and temperature conditions. The solubility of CO_2 in water or brine is computed using routines from ECO2N (Pruess, 2005), a fluid property module for the TOUGH2 simulator (Version 2.0) that was designed for applications to geologic sequestration of CO_2 in saline aquifers. ECO2N implements the mutual H_2O-CO_2 solubility model of Spycher et al. (2003) and Spycher and Pruess (2005), which was thoroughly tested against a large number of experimental data. As done by Spycher et al. (2003) for CO_2, the solubility of H_2S in water is computed using "true" equilibrium constants (K) (i.e., directly related to the standard Gibbs free energy of reaction) rather than Henry's law constants (K_H). At equilibrium, the following reaction and corresponding equilibrium constant can be written:

$$H_2S_{(g)} \Leftrightarrow H_2S_{(aq)} \quad K = a_{H2S(aq)} / f_{H2S(g)}$$

where K is the equilibrium constant (pressure P and temperature T-dependent), f is fugacity in the gase phase (P, T, and composition dependent), and a is activity in the aqueous phase (P, T, and composition dependent as well). The thermodynamic model

presented by Duan et al. (2007) was used to calculate effective values of *K* as a function of temperature, pressure, and salinity, while the fugacity was computed using the modified SRK equation of state and parameters implemented into GASEOS.

4.2. Model results

A period of 3.5 years of CO_2+H_2S injection is simulated, until the plume reaches the left model boundary in the overlying aquifer. The movement of the "gas" plume is similar to that shown earlier for the case of pure CO_2 injection (Figure 2). After injection starts, the resulting plume accumulates at the top of the storage formation, moving both down- and upgradient from the injection point. When it encounters the fracture zone, it migrates upward, enters the overlying aquifer, and spreads out laterally into the shallow aquifer.

The computed spatial distribution of H_2S mass fraction in the supercritical fluid plume (compressed "gas" phase) is shown in Figure 6 (a). The preferential dissolution of H_2S in the aqueous phase strips H_2S from the edge of the advancing plume. Such preferential dissolution is more significant upgradient (left side of the plume), owing to the influx of H_2S-undersaturated water. Along the path from the injection point to the fracture zone where the plume continuously moves, the mass fraction of H_2S in the plume remains more or less constant and at the same value as the mass fraction at the injection point. As the gaseous H_2S is stripped from the edge of the gas plume, the mass fraction of CO_2 in the gas phase increases correspondingly (Figure 6b), thus showing the enrichment of CO_2 in the gas phase (relative to H_2S) caused by this chromatographic partitioning.

Eventually, a gaseous CO_2+H_2S mixture with the same proportion of each component as the injected mixture is predicted to migrate through the fracture and to enter the overlying aquifer (Figure 6); however, the arrival of H_2S is delayed. Figure 7 shows the time evolution of the H_2S mass fraction in the plume at the bottom of the fracture zone where it connects to the storage formation (point A), and at the top of the fracture zone where it connects to the overlying aquifer (point B). The plume is predicted to arrive at point A after 0.84 years, migrate upward in the fracture, and arrive at point B after 2.05 years. The breakthrough curves for H_2S show different trend for points A and B. The breakthrough curve at point A is characterized by a sharp initial increment in mass fraction followed by a slow increase after the mass fraction of H_2S rises to about 0.04. The breakthrough curve at point B shows mass fractions that remain small at first (close to 0%, which means the arriving gas phase contains almost pure CO_2), then sharply increase about 4 months after the plume first arrives, and eventually reach a plateau value close to 0.05 (the mass fraction of H_2S in the injected stream). As seen from Figures 6 and 7, the breakthrough of H_2S is delayed, and the extent of the delay depends on travel distance and depth of the observation point (at point B, the plume contains nearly pure CO_2 for about 4 months).

5. Impact of co-injected H_2S on the quality of a fresh water aquifer

The model simulations presented earlier indicate that the breakthrough of H_2S co-migrating with CO_2 along a preferential pathway may be delayed compared to the arrival of the bulk compressed "gas" phase. At some point in time, however, the ratio of H_2S to CO_2 in the leaking compressed "gas" reaching an overlying aquifer is predicted to approach the same level as in the injected gas mixture. Therefore, the extent to which a leak of CO_2+H_2S (compared to a leak of pure CO_2) would affect groundwater warrants further investigation. Obviously, the presence of H_2S in water itself is a water quality issue, because of its high toxicity at elevated concentrations, "rotten egg" odor at low concentrations, and potential for oxidation to sulfuric acid resulting in acidification and further degradation of water quality. A concentration limit of dissolved H_2S is not included in the EPA National Primary Drinking Water Regulations (the legally enforceable standards). However, a standard is specified in the National Secondary Drinking Water Regulations (the non-enforceable guidelines regulating contaminants) as three times the threshold odor number (TON), which is variable but typically in the ppb range for water (e.g., Amoore and Hautala, 1983). Therefore, the leakage of H_2S with CO_2 could easily lead to concentrations exceeding this low limit.

Simulations are presented below to investigate potential effects of trace H_2S leaking with CO_2, focusing on thiophillic elements lead and arsenic in an anoxic environment.

Considering the effects of H_2S oxidation by groundwater or atmospheric O_2 was deemed beyond the scope of this study. Here, our main purpose is to compare model results for a case of CO_2+H_2S leakage with a case reported earlier involving only CO_2 (Zheng et al., 2009), for a very simplified "generic" aquifer, considering trace metals in solid solution with sulfide minerals as well as sorbed onto Fe(III) hydroxides.

5.1. Model Setup

The same model setup as that presented earlier by Zheng et al. (2009) and Apps et al. (2010) is used as a base case, the only difference being that a CO_2+H_2S mixture (instead of CO_2 alone) intrudes into the aquifer, consequently allowing direct comparison of model results for the base case (H_2S+CO_2) with earlier model results (CO_2 only). It should be noted that the assumed temperature and pressure conditions in the simulated aquifer in this case are 25°C and 5 bar.

The model setup representing the shallow aquifer is shown in Figure 8. It consists of a horizontal two-dimensional domain with a thickness Δz =10 m, with spatial discretization Δx =10 m and Δy = 10 m. The hydrogeological properties, as given in Table 2, are homogeneous and constant in time. The initial chemical composition of groundwater is given in Table 3, and was taken from Zheng et al. (2009). The host mineralogy of the aquifer is similar to that used therein (Appendix A), except that orpiment (As_2S_3) and (As_4S_4) are added to the list of potential secondary minerals that could form in cases of high sulfide concentrations.

Chemical reactions considered in the model include aqueous complexation, mineral dissolution/precipitation, and adsorption/desorption via surface complexation. Surface complexation reactions and their equilibrium constants for lead and arsenic on different minerals are listed in Appendix B. The model assumes that As and Pb are initially present in sediments as sulfide minerals (arsenian pyrite and galena) as well as sorbed species onto goethite and clays (Table 4). Arsenian pyrite is represented with the following reaction stoichiometry (where $O_{2(aq)}$ is used to thermodynamically balance electrons but is not a major component; see Zheng et al., 2009):

$$FeAs_{0.05}S_{1.95} + 1.025\ H_2O + 0.0375\ O_2(aq) = 1.0000\ Fe^{+2} + 0.1875\ H^+ + 0.2375\ SO_4^{-2} + 1.7125\ HS^- + 0.0500\ H_3AsO_3(aq)$$

As shown in Table 4, more than 99% percent of the lead is assumed to reside initially in galena. In contrast, adsorbed arsenic accounts for about 63% of the total initial mass of arsenic, which implies that the desorption of arsenic could have a larger impact than the desorption of lead. Computed initial total loadings of these metals in the sediments (i.e., solid+sorbed) are about 28 ppm of arsenic and 10 ppm of lead. These concentrations compare with average crustal abundance of about 2 ppm arsenic and 14 ppm lead (estimated Birkholzer et al., 2008) and typical concentrations in rock from various areas of the United States of 1.1–4.3 ppm arsenic and 5–17 ppm lead in sandstones, and 6.4–9.0 ppm arsenic and 11–24 ppm lead in shales (Connor and Shacklette, 1975). Therefore, in the present study, the assumed abundance of arsenic in sediments may be rather high,

and thus expected to result in overestimated, rather than underestimated, predicted arsenic concentrations upon mobilization by H_2S- and CO_2-laden waters.

The geochemical thermodynamic database used here is the EQ3/6V7.2b database (Wolery, 1993) with augmentation of arsenic oxyanions and arsenic and lead sulfide and selenide oligomeric complexes compiled from an earlier literature review (Birkholzer et al., 2008). Most constants are from this database with equilibrium constants for orpiment and realgar from Spycher and Reed (1989). The minerals and their kinetic data are given Appendix B.

5.2. Model Results

The total mass of the CO_2+H_2S gas mixture leaking into the aquifer is 7.9×10^{-5} kg/s, 95% of which is CO_2 and 5% is H_2S. This leakage rate is slightly higher than the pure-CO_2 injection rate assumed in Zheng et al. (2009) (7.5×10^{-5} kg/s); however, the spatial distribution of the gas phase is almost identical to that obtained for the case with pure CO_2.

Our simulations address the question of whether the presence of H_2S in the gas mixture could exacerbate previously predicted CO_2 impacts on shallow groundwater, as far as metal release from sediments. The dissolution of H_2S in water increases the acidity of the solution because of deprotonation, as revealed in the following reaction—

$$H_2S(g) = H^+ + HS^-$$

However the reductive dissolution of Fe(III) (hydr)oxides (Palandri and Kharaka, 2005; Palandri et al., 2005) as expressed by the following reaction:

$$FeOOH(goethite) + 1.875H^+ + 0.125HS^- = Fe^{+2} + 0.125SO_4^{2-} + 1.5H_2O$$

consumes more proton than that being released by the dissolution of H_2S and subsequently further buffers pH. The precipitation of pyrite buffers pH as well. As a result, the pH of the groundwater in case of the leakage of an H_2S+CO_2 mixture (Figure 9) is slightly higher than the case of a pure-CO_2 leakage.

The spatial distribution of elevated aqueous sulfide (Figure 10) concentration is constrained by the precipitation of pyrite (Figure 11), which also indicates that pyrite precipitation sequesters a significant amount of sulfide. The total aqueous sulfide concentration consistently peaks at the injection locations (Figure 10), but the magnitude of the concentration at the peak decreases gradually as the rate of pyrite precipitation increases (the more pyrite forms, the larger the surface area it has and therefore the faster is the precipitation rate).

The ferrous iron needed for the precipitation of pyrite comes from the reduction of ferric iron in goethite by aqueous sulfide. Pyrite precipitation competes with siderite precipitation for ferrous iron released by goethite dissolution. Also, a comparison

between Figure 11 and 12 reveals that siderite precipitates in areas where pyrite precipitation is impeded by low aqueous sulfide concentrations. Note that increasing the dissolution rate of goethite can yield overlapping precipitation of both pyrite and siderite (Zheng et al., 2010). This observation is in line with modeling findings by Palandri and Kharaka (2005), who show that the precipitation of pyrite progressively overlaps with the precipitation of siderite as the molar ratio of sulfur (SO_2 in their case) to CO_2 is increased. Batch experiments reacting hematite and CO_2 with SO_2 (Palandri et al., 2005) and sodium sulfide (Murphy et al., 2011) revealed the precipitation of both siderite and Fe sulfides, while similar experiments using ferrihydrite instead of hematite (Murphy et al., 2010) lead to the precipitation of elemental sulfur instead of Fe sulfides. This points to the effects of competing rates of Fe(II) and sulfide supply and consumption. Whether Fe(II) precipitates as pyrite preferentially to siderite depends on the relative precipitation rates of these minerals, the rate of precipitation of these minerals relative to the goethite dissolution rate, and whether elemental sulfur is allowed to precipitate or not. Here, for simplicity, sulfur precipitation is not considered, and although the precipitation of amorphous iron sulfide (FeS) is favored kinetically, it is not modeled on the basis that pyrite would eventually replace initially precipitated FeS. It should also be noted that in the experiments of Palandri et al. (2005), the abundance of iron (hydr)oxides is much higher than considered in our model, presenting more surface area, thus likely increasing the effective dissolution rates of these minerals.

The predicted (total) aqueous concentration of lead at different times is shown on Figure 13a. The interplay between desorption (increasing aqueous lead concentration) and

precipitation of galena (decreasing aqueous lead concentration) controls the spatial distribution of lead. A maximum peak concentration is observed at the intrusion location after 3.5 years, caused by fast (equilibrium) desorption coupled with slower precipitation of galena under kinetic constraints. With time, as the plume of elevated hydrogen sulfide propagates downgradient, the concentrations of lead decrease to very low values, owing to precipitation of galena with a more-than-sufficient supply of aqueous sulfide. A peak continues to show only at the tip of the aqueous sulfide plume, where the precipitation of galena is slower than the fast release of lead from sorption sites. The intensity of this peak, however, decreases with travel distance, to a point at which the lead concentration after 50 or 100 years is just about twice that of the initial concentrations. Model results show that the peak of lead concentration is significantly higher than the initial concentration (Figure 13a).

The maximum aqueous lead concentrations obtained here for leakage of CO_2+H_2S mixtures is similar to that for the pure CO_2 leakage case in Zheng et al. (2009). The reason is that the lead sorbed on minerals surfaces is the main source for the increase in aqueous lead concentration, and that the initial amount of lead residing on the mineral surfaces is very similar in both cases. In the pure CO_2 intrusion simulation (Zheng et al., 2009), galena precipitation occurs under most simulation conditions due to the release of lead from sorption sites, whereas galena dissolution occurs only when the concentration of sorption sites is very low. In the simulations with H_2S+CO_2 mixtures, the possibility of galena dissolution is essentially ruled out, because the increase in hydrogen sulfide

triggers the precipitation of galena regardless of whether lead is released from sorption sites or not.

Figure 14 shows the profile of total adsorbed arsenic concentration. As shown in this figure, desorption is most significant at the intrusion location. A substantial amount of arsenic is released into the aqueous phase and transported downgradient (Figure 15). The aqueous complexation of arsenic with sulfide (e.g., Helz and Tossell, 2008) results in a much higher aqueous arsenic concentration than that for pure CO_2 leakage case in Zheng et al. (2009) (Figure 15). As the groundwater plume with higher arsenic concentration moves downgradient, adsorption occurs at the edge of the plume (Figure 14) which lowers the concentration of arsenic at this location.

As a result of the high arsenic concentrations and the elevated sulfide concentrations, both arsenian pyrite and orpiment precipitate (Figure 16). The prominent desorption of arsenic results in high concentrations of arsenic in the aqueous phase (Figure 15), despite the precipitation of arsenian pyrite and orpiment. However, in this case, orpiment (As_2S_3) is assumed to form at a rather slow rate (Table A1). Because elevated arsenic concentration in sulfidic waters are typically limited by orpiment solubility, additional simulations assuming orpiment to form at equilibrium were also conducted. These simulations show aqueous As concentrations about two orders of magnitude lower than in the present case. Furthermore, the amount of metals released from the sediments, and therefore the resulting aqueous concentrations, also largely depend on the initial concentration of metals in the sediments (Table 4). As noted earlier, the initial loading of

arsenic in this case is on the high side, and thus is expected to yield predicted dissolved concentrations that are rather too high than too low.

6. Summary and Conclusion

In this study, reactive transport simulations were used to assess the mobilization and transport of organics with supercritical CO_2 (SCC), and the co-injection and transport of H_2S with SCC. These processes were evaluated at conditions of typical storage reservoirs, and for cases of hypothetical leakage from a reservoir to an overlying shallower aquifer. The simulations are intended to help evaluate and understand various processes at play, in a more qualitative than quantitative manner, and only for hypothetical scenarios.

Numerical simulations were conducted to evaluate the possible mobilization of organics by SCC (with benzene as a proxy compound) from a deep storage formation to an overlying aquifer. Model results show that benzene preferentially partitions into SCC, and therefore could be depleted from deep formations and transported by SCC. Given that SCC is a known solvent for organic compounds, these results by themselves are not surprising. One important question is whether the transport of organics (benzene in this case) by SCC along a leakage pathway could impact overlying aquifers. Because SCC is buoyant in water, it has the potential to migrate upward through a fault or another preferential pathway. The mutual solubilities of the components involved (CO_2, benzene, and water) change as a function of pressure and temperature, and therefore the partitioning behavior changes along the flow path. Our results suggest that under the

conditions modeled here, benzene could co-migrate with CO_2 into an overlying aquifer if a leakage pathway were present. Because the aqueous solubility of benzene in contact with CO_2 is lower than the aqueous solubility of CO_2, benzene is continuously enriched at the front of the advancing SCC plume. For the case studied here, which considered a 1100 m long preferential pathway, the predicted aqueous benzene concentration mobilized by SCC leakage to the overlying aquifer is on the same order of magnitude as the initial benzene concentration in the storage formation. However, re-sorption of organics along the leakage pathways or within the impacted aquifer was not considered, likely overestimating the mobilization potential. Our simulations in this case are mainly intended to illustrate a case of mobilization, and demonstrate potentially useful modeling capabilities that could be applied to real systems. Although this study considered, as an example, trace benzene concentrations in a deep formation, leaching of potentially larger amounts of organic compounds from organic-matter-rich reservoir clay caps should also be considered when evaluating the risk of groundwater contamination above storage reservoirs. If models were used to evaluate the risk associated with organic compound, our confidence level would be higher if the following type of data is available: the concentration of BETX, phenol, PAHs in saline water and their abundance in solid phase, their partition coefficient under relevant pressure and temperature, and sorption capacity of organics in the caprock.

Like benzene, the fate of H_2S in a storage formation and its behavior along a potential leakage pathway are controlled by chromatographic partitioning between the gas (CO_2) and the aqueous phase (brine). Because the solubility of H_2S in water is higher than its

solubility in SCC, H_2S tends to become depleted from the CO_2 phase as the SCC plume advances. The main question in this case is whether H_2S could be completely stripped out of the SCC plume before it reaches an overlying aquifer. Model results suggest that leakage pathways may allow co-migration of CO_2+H_2S despite the preferential dissolution (stripping) of H_2S at the edge of the advancing CO_2+H_2S plume. Some delay is predicted between the CO_2 and H_2S times of arrival (into the shallow aquifer) caused by the preferential dissolution of H_2S over CO_2, although in our case this effect is temporary. At some point the effect of H_2S stripping by groundwater is no longer noticeable, and H_2S co-migrating with CO_2 enters the aquifer at about the same concentration as in the CO_2 stream injected into the deep formation. These results are expected to depend strongly on length of the leaking period and of the rate of fluid migration (mostly by advection) along the leakage pathway relative to the rate of migration/dissipation horizontally away from the pathway (typically mostly by diffusion). The relative extent of these processes depends on the respective hydrological properties of flow pathways and their surroundings. In this respect, our simulations are only showing that H_2S could break through into a shallow aquifer under some conditions, and by no means indicate that this outcome would be expected under all leakage conditions.

In addition to potentially adverse effects of H_2S itself (i.e., odor and taste), our simulations suggest that the leakage of CO_2+H_2S into an anoxic aquifer could lead to higher arsenic release in groundwater than for cases of pure CO_2 leakage scenario (e.g, Zheng, 2009) because of the formation of stable As-sulfide aqueous species. Obviously, the use of models alone to investigate an aquifer response to intrusion of CO_2+H_2S

mixtures (or even just CO_2) is seriously limited, because such response depends on site specific conditions such as metal-sediment associations, groundwater composition and redox conditions, leakage rate versus regional groundwater flow rates, and many other hydrologic and geochemical parameters. Here we have considered trace metals associated with sulfide minerals as well as sorbed onto Fe(III) hydroxides in an anoxic environment. Ongoing field and laboratory investigations by our group (Zheng et al., 2012; Trautz et al., 2012)and others (Marcon et al., 2012)since the present study was conducted have shown that ion exchange and dissolution of minerals such as carbonates and clays are other mechanisms potentially leading to the release of metals in aquifers impacted by CO_2. It should be noted that a recent field test involving the carbonation of a strongly reducing groundwater aquifer containing As and Pb-bearing sulfide minerals (Trautz et al., 2012) showed no noticeable As and Pb release after five months of injection of CO_2-saturated groundwater, but release of Fe and alkaline earth metals attributed to ion exchange and/or desorption, or possibly to dissolution of Fe(II) sulfides, Fe(III) (hydr)oxides, clays, and/or trace carbonates. These studies point out the difficulty of generalizing anticipated effects of CO_2 leakage on groundwater quality and the need for more site specific studies. Nevertheless, purely exploratory simulations such as those presented here are useful to investigate couplings between various hydrogeochemical processes and their potential effects on groundwater quality, and in doing so help guide research directions for more specific field and laboratory studies.

Appendix A

The mass transfer between the aqueous and solid phases is a key process for leaching of benzene by CO_2. The K_d approach is used to calculate the release of adsorbed benzene into the aqueous phase via the surface complexation model (SCM) capability implemented into TMVOC_REACT. This requires the conversion of K_d values to K_{SCM} values, which represent sorption intrinsic equilibrium constants input into the simulator. Basically, the following reaction applies:

$$SOH\_C_6H_6 \rightleftharpoons C_6H_6(aq)+SOH \quad \text{(A1)}$$

where $_{SOH\_C_6H_6}$ is sorbed benzene concentration (the "surface complex") and SOH is the concentration of unoccupied sorption sites, both in units of mol/kg_{water}. The (intrinsic) sorption constant is then given as:

$$K_{scm} = \frac{[C_6H_6][SOH]}{[SOH\_C_6H_6]} \quad \text{(A2)}$$

where brackets represent concentration (mol/kg_{water}), assuming ideal solution behavior. The total concentration of sorption sites is equal to the sum of [$SOH\_C_6H_6$] and [SOH]. Considering that [$SOH\_C_6H_6$] is much smaller than [SOH], the total concentration of sorption sites is roughly the same as [SOH]. The total mass of sorbing organic matter (m^s_{oc}) and the mass of sorbed benzene (m^S_i) can then be related directly to [SOH] and [$SOH\_C_6H_6$] by:

$$\frac{[\mathrm{SOH}]}{[\mathrm{SOH\_C_6H_6}]} = \frac{m_{oc}^{S} / f_{oc} \cdot Sd \cdot A}{m_i^{S} / W} \tag{A3}$$

where Sd is sorption site density (mol/m^2), A is specific surface area of the sorbent (m^2/g) and W is the molecular weight of benzene. By combining Equations A2 and A3 the sorption constant K_{scm} can then be related to K_{oc} as follows:

$$\mathrm{K_{SCM}} = \frac{[C_6H_6(aq)][\mathrm{SOH}]}{[\mathrm{SOH\_C_6H_6}]} = m_i^{H_2O} / m^{H_2O} \times 1000 / W \cdot \frac{m_{oc}^{S} / f_{oc} \cdot Sd \cdot A}{m_i^{S} / W} = m_i^{H_2O} / m^{H_2O} \times 1000 / W \cdot \frac{Sd \cdot A \cdot W}{f_{oc} \cdot m_i^{S} / m_{oc}^{S}}$$
$$= 1000 \cdot \frac{Sd \cdot A}{f_{oc} \cdot \frac{m_i^{S} / m_{oc}^{S}}{m_i^{H_2O} / m^{H_2O}}} = 1000 \cdot \frac{Sd \cdot A}{f_{oc} \cdot K_{oc}} \tag{A4}$$

Therefore, as shown in Equation (A4), one needs to estimate values of *Sd, A, K_{oc} and* f_{oc} to calculate values of K_{scm} for input into the model. Baldi and Bargagli (1982) measured the specific area of marine sediments ranging from 10 to 40 m^2/g. Kulp and Carr (1952) reported specific surface areas of deep-sea sediment ranging from 2.5 to 48 m^2/g. Based on these values, we assume a specific surface area of 10 m^2/g. A site density of 10^{-6} mol/m^2 is used as a starting point to yield an assumed 1×10^{-4} ppm benzene in the soil (about 0.01 ppm in kerogen) at an aqueous benzene concentration of 0.001 mg/L. A K_{oc} value of 1.9 is selected (Karickhoff et al., 1979). Considering that f_{oc} values for natural or uncontaminated soil ranges from 0.0006 to 0.013 (Larsen et al., 1992, Donahue et al., 1999), we assume a value of 0.01. Using these assumed values for *Sd, A,* K_{oc} and f_{oc}, the calculated log K_{scm} based on Equation (A4) is –1.9. These data correspond to an initial

aqueous benzene concentration of 1.28×10^{-8} mol/kg_{water} (~0.001 mg/L), and adsorbed benzene concentration of 1.23×10^{-8} mol/kg_{water} (corresponding to 1×10^{-4} ppm in the sediment, and corresponding to 0.01 ppm in kerogen).

Appendix B

Table B1 shows the kinetic data adopted for all the minerals included in the simulation. Kinetic rate parameters for most rock-forming minerals were taken from Palandri and Kharaka (2004), which are based mainly on experimental studies conducted under far-from-equilibrium conditions. The mineral reactive-surface areas were taken from Xu et al. (2007; 2006), based on the work of Sonnenthal et al. (2005). A thorough review and discussion of the kinetic rates for arsenian pyrite, pyrite, and galena was given in Zheng et al. (2009). The kinetic rates for orpiment and realgar were arbitrarily taken to be the same as those for arsenian pyrite. Tables B2 and B3 shows the surface complexation of lead and arsenic on different minerals.

Acknowledgment

This work was supported by the Assistant Secretary for Fossil Energy, Office of Sequestration, Hydrogen, and Clean Coal Fuels, through the National Energy Technology Laboratory, U.S. Department of Energy, under Contract No. DE-AC02-05CH11231.

References

Aiuppa, A., C. Federico, P. Allard, S. Gurrieri and M. Valenza, 2005. Trace metal modeling of groundwater-gas-rock inter-actions in a volcanic aquifer: Mount Vesuvius, Southern Italy. Chemical Geology, 216: 289-311.

Amoore J.E., and E. Hautala, 1983. Odor as an aid to chemical safety: Odor thresholds compared with threshold limit values and volatilities for 214 chemicals in air and water dilution. J. Appl. Toxicol. 3(6):272-290.

Arnórsson, S., Hurtig, N., Gysi, A. P., Bird, D. K. and O'Day, P. A., 2010. Carbon dioxide waters in Iceland: A natural analogue to CO_2 sequestration in basaltic aquifers. Water-Rock Interaction. Birkle and Torres-Alvarado. Guanajuato, Mexico, 2010 Taylor & Francis Group, London, ISBN 978-0-415-60426-0.

Anitescu, G. and L.L. Tavlarides, 2006. Supercritical extraction of contaminants from soils and sediments. J. of Supercritical Fluids, 38: 167-180.

Appelo, C.A.J., M.J.J. Van Der Weiden, C. Tournassat and L. Charlet, 2002. Surface complexation of ferrous iron and carbonate on ferrihydrite and the mobilization of arsenic. Environ. Sci. Technol., 36(14): 3096-3103.

Apps, J. A., Zheng, L., Zhang, Y., Xu, T. and Birkholzer, J. T., 2010. Evaluation of groundwater quality changes in response to CO2 leakage from deep geological storage. Transport in Porous Media 82(1): 215-246.

Bachu, S. and D.B. Bennion, 2009. Chromatographic partitioning of impurities contained in a CO_2 stream injected into a deep saline aquifer: Part 1. Effects of gas

composition and in situ conditions. International Journal Of Greenhouse Gas Control, 3(4): 458-467.

Bachu, S., M. Pooladi-Darvish and H.F. Hong, 2009. Chromatographic partitioning of impurities (H2S) contained in a CO_2 stream injected into a deep saline aquifer: Part 2. Effects of flow conditions. International Journal Of Greenhouse Gas Control 3(4): 468-473.

Birkholzer, J.T., J.A. Apps, L. Zheng, Y. Zhang, T. Xu and C.-F. Tsang., 2008. Research project on co_2 geological storage and groundwater resources: water quality effects caused by co_2 intrusion into shallow groundwater. Technical Report LBNL-1251E, Lawrence Berkeley National Laboratory, Berkeley, CA.

Bondor, P.L., 1992. Applications of carbon dioxide in enhanced oil recovery. Energy Conversion & Management 33(5-8): 579-586.

Bradbury, M. H. and B. Baeyens, 2005. Modelling the sorption of Mn(II), Co(II), Ni(II), Zn(II), Cd(II), Eu(III), Am(III), Sn(IV), Th(IV), Np(V) and U(VI) on montmorillonite: Linear free energy relationships and estimates of surface binding constants for some selected heavy metals and actinides. Geochimica et Cosmochimica Acta, 69(4): 875-892.

Carroll, S., Hao, Y. and Aines, R., 2009. Geochemical detection of carbon dioxide in dilute aquifers. Geochemical Transactions 10(4), 1-18.

Deeds, N.E., D.C. McKinney and G.A. Pope, 2000. Laboratory characterization of non-aqueous phase liquid/tracer interaction in support of a vadose zone partitioning interwell tracer test. J. Contaminant Hydrol., 41: 193-204.

Dixit, S. and J.G. Hering, 2003. Comparison of arsenic(v) and arsenic(iii) sorption onto iron oxide minerals: implications for arsenic mobility. Environ. Sci. Technol. 37: 4182-4189.

Doughty, C. and K. Pruess, 2005. Modeling supercritical carbon dioxide injection in heterogeneous porous media. Vadose Zone Journal, 3(3): 837-847.

Duan, Z., R. Sun, R. Liu and C. Zhu, 2007. Accurate thermodynamic model for the calculation of h_2s solubility in pure water and brines. Energy & Fuels, 21: 2056-2065.

Flaathen, T. K., Gislason, S. R., Oelkers, E. H. and Sveinbjörnsdóttir, Á. E., 2009. Chemical evolution of the Mt. Hekla, Iceland, groundwaters: A natural analogue for CO_2 sequestration in basaltic rocks. Applied Geochemistry 24(3), 463-474.

Freund, H. and S.R. Kelemen, 1989. Low-temperature pyrolysis of Green River kerogen. AAPG Bulletin, 73: 1011-1017.

Ghonasgi, D., S. Gupta, K.M. Dooley and F.C. Knopf, 1991. Supercritical CO2 extraction of organic contaminants from aqueous streams. AIChE J., 37.

Green, L.A. and A. Akgerman, 1996. Supercritical co_2 extraction of soil-water slurries. The Journal of Supercritical Fluids, 9(3): 177-184.

Gu, X. and L.J. Evans, 2007. Modelling the adsorption of Cd(II), Cu(II), Ni(II), Pb(II), and Zn(II) onto Fithian illite. Journal of Colloid and Interface Science 307, 317-325.

Gunter, W.D., E. H. Perkins and I. Hutcheon, 2000. Aquifer disposal of acid gases: modeling of water-rock reactions for trapping of acid wastes. Appl. Geochem. 15 (8), 1085–1095.

Gunter, W.D., A. Pratt, B.E. Buschkuehle and E.H. Perkins, 2005. Acid gas injection in the Brazeau Nisku Q carbonate reservoir: Geochemical reactions as a result of the injection of an H_2S-CO_2 waste stream. Greenhouse Gas Control Technologies 7, 469-477

Hauthal, W.H., 2001. Advances with supercritical fluids [review]. Chemosphere, 43: 123-135.

Hizal, J. and R. Apak, 2006. Modeling of copper(II) and lead(II) adsorption on kaolinite-based clay minerals individually and in the presence of humic acid. Journal of Colloid and Interface Science 295, 1-13.

Illiassov, P.A. and A. Datta-Gupta, 2002. Field-scale characterization of permeability and saturation distribution using partitioning tracer tests: the Ranger Field, Texas. SPE Journal, 7(4): 409-420.

Keating, E. H., Fessenden, J., Kanjorski, N., Koning, D. J. and Pawar, R., 2010. The impact of CO_2 on shallow groundwater chemistry: observations at a natural analog site and implications for carbon sequestration. Environmental Earth Sciences 60(3), 521-536.

Kharaka, Y.K. and J.S. Hanor, 2007. Deep fluids in the continents: I. sedimentary basins. In: J.I. Drever (Editor), Surface and Ground Water, Weathering and Soils. Elsevier, Treatise on Geochemistry, pp. 1-48.

Kharaka , YK , Thordsen , JJ , Hovorka , SD , Nance , HS , Cole , DR , Phelps , TJ and Knauss , KG. (2009) Potential environmental issues of CO 2 storage in deep saline aquifers: Geochemical results from the Frio - I brine pilot test, Texas, USA. Applied Geochem. 24 : 1106 – 12 .

Kharaka, Y.K, J.J. Thordsen, E. Kakouros, G. Ambats, W.N. Herkelrath, J.T. Birkholzer, J.A. Apps, N.F. Spycher, L. Zheng, R.C. Trautz, H.W. Rauch, and K. Gullickson, K. (2010) Changes in the chemistry of shallow groundwater related to the 2008 injection of CO2 at the ZERT Field Site, Bozeman, Montana. Environmental Earth Sciences, 60 (2), 273–284

Knauss, K.G., J.W. Johnson and C.I. Steefel, 2005. Evaluation of the impact of CO_2, co-contaminant gas, aqueous fluid and reservoir rock interactions on the geologic sequestration of CO_2. Chemical Geology, 217: 339-350.

Kraemer, T.F. and D.F. Reid, 1984. The occurrence and behavior of radium in saline formation water of the U.S. gulf coast region. Isotope Geoscience, 2: 153-174.

Lammers, K., R. Murphy, A. Riendeau, A. Smirnov, M. A. A. Schoonen and D. R. Strongin 2011. CO2 Sequestration through Mineral Carbonation of Iron Oxyhydroxides. Environmental Science & Technology 45(24): 10422-10428.

Little, M. G. and Jackson, R. B., 2010. Potential impacts of leakage from deep co_2 geosequestration on overlying freshwater aquifers. Environmental Science & Technology 44(23), 9225-9232.

Lu, J. M., Partin, J. W., Hovorka, S. D. and Wong, C., 2010. Potential risks to freshwater resources as a result of leakage from CO_2 geological storage: a batch-reaction experiment. Environmental Earth Sciences 60(2), 335-348.

Marcon,V., J. Kaszuba1, A. Navarre- Sitchler and K. Mouzakis, 2012, Mobilization of Trace Metals with Carbon Sequestration and Potential Impacts on Groundwater, 11th annual conference of Carbon Capture, Utilization & Sequestration, April 30 - May 3, Pittsburgh, PA.

McGrath, A. E., G. L. Upson and M. D. Caldwell 2007. Evaluation and Mitigation of Landfill Gas Impacts on Cadmium Leaching from Native Soils. Ground Water Monitoring & Remediation 27(4): 99-109.

Manning, B.A. and S. Goldberg, 1997. Adsorption and stability of Arsenic(III) at the clay mineral-water interface. Environ. Sci. Technol. 31, 2005-2011.

McAuliffe, C., 1969. Determination of dissolved hydrocarbons in subsurface brines. Chemical Geology, 4: 225-233.

Moridis, G.J., M.B. Kowalsky, and K. Pruess, 2008. TOUGH+HYDRATE v1.0 user's manual: a code for the simulation of system behavior in hydrate-bearing geologic media, Report LBNL-00149E, Lawrence Berkeley National Laboratory, Berkeley, CA.

Muller, B. and L. Sigg, 1991. Adsorption of lead(ll) on the goethite surface: voltammetric evaluation of surface complexation parameters. Journal of Colloid and Interface Science 148(2), 517-532.

Murphy, R., K. Lammers, A. Smirnov, M. A. A. Schoonen and D. R. Strongin 2010. Ferrihydrite phase transformation in the presence of aqueous sulfide and supercritical CO2. Chemical Geology 271(1-2): 26-30.

Murphy, R., K. Lammers, A. Smirnov, M. A. A. Schoonen and D. R. Strongin 2011. Hematite reactivity with supercritical CO2 and aqueous sulfide. Chemical Geology 283(3-4): 210-217.

Orbey, H. and S.I. Sandler, 1998. Modeling vapor-liquid equilibria: cubic equations of state and their mixing rules. Cambridge University Press.

Palandri, J. and Y.K. Kharaka, 2004. A compilation of rate parameters of water-mineral interaction kinetics for application to geochemical modeling. Open File Report 2004-1068, US Geological Survey.

Palandri, J.L. and Y.K. Kharaka, 2005. Ferric iron-bearing sediments as a mineral trap for CO_2 sequestration: Iron reduction using sulfur-bearing waste gas. Chemical Geology, 217: 351-364.

Palandri, J.L., R.J. Rosenbauer and Y.K. Kharaka, 2005. Ferric iron in sediments as a novel CO_2 mineral trap: CO_2–SO_2 reaction with hematite. Applied Geochemistry, 20: 2038-2048.

Pruess, K., 2005. ECO2N: A TOUGH2 Fluid property module for mixture of water, NaCl, and CO_2. LBNL-57592, Lawrence Berkeley National Laboratory, Berkeley, CA.

Pruess, K. and A. Battistelli, 2002. TMVOC, a numerical simulator for three-phase non-isothermal flows of multicomponent hydrocarbon mixtures in saturated–unsaturated heterogeneous media, Lawrence Berkeley National Laboratory, Berkeley, CA.

Pruess, K., C. Oldenburg and G. Moridis, 1999. TOUGH2 user's guide, version 2.0. LBL-43134, Lawrence Berkeley National Laboratory, Berkeley, CA.

Reagan, M.T. and C.M. Oldenburg, 2006. WebGasEOS v1.0 User Guide, LBNL-3188, (June 2006).

RøeUtvik, T.I., 1999. Chemical characterization of produced water from four offshore oil production platforms in the North Sea. Chemosphere, 39: 2593–2606.

Silin, D., T. Patzek and S. Benson, 2009. A model of buoyancy-driven two-phase countercurrent fluid flow. Transport in Porous Media, 76(3): 449-469.

Sirivedhin, T. and L. Dallbauman, 2004. Organic matrix in produced water from the Osage-Skiatook Petroleum Environmental Research site, Osage county, Oklahoma. Chemosphere, 57 463–469.

Smyth, R.C., S.D. Hovorka, J. Lu, K.D. Romanak, J.W. Partin, C. Wong and C. Yang, 2009. Assessing risk to fresh water resources from long term CO_2 injection – laboratory and field studies. Energy Procedia, 1(1957-1964).

Smyth, T.J., R.G. Zytner and W.H. Stiver, 1999. Influence of water on the supercritical fluid extraction of naphthalene from soil. Journal of Hazardous Materials, 67(2): 183-196.

Sonnenthal, E., A. Ito, N. Spycher, M. Yui, J. Apps, Y. Sugita, M. Conrad and S. Kawakami, 2005. Approaches to modeling coupled thermal, hydrological, and chemical processes in the Drift Scale Heater Test at Yucca Mountain. Int. J. Rock Mech. Min. Sci., 42: 6987–719.

Spycher, N. and K. Pruess, 2005. CO_2-H_2O mixtures in the geological sequestration of CO_2. II. Partitioning in chloride brines at 12–100°C and up to 600 bar. Geochimica et Cosmochimica Acta, 69(13): 3309-3320.

Spycher, N., K. Pruess and J. Ennis-King, 2003. CO_2-H_2O mixtures in the geological sequestration of CO_2. I. Assessment and calculation of mutual solubilities from 12 to 100°C and up to 600 bar. Geochimica et Cosmochimica Acta, 67(16): 3015-3031.

Spycher, N. and M.H. Reed, 1989. Evolution of a broadlands-type epithermal ore fluid along alternative P-T paths: implications for the transport and deposition of base, precious, and volatile metals. Economic Geology, 84: 328-359.

Tang, J.S., 2005. Extended Brigham model for residual oil saturation measurement by partitioning tracer tests. SPE Journal, 10(2): 175-183.

Trautz, R. C., J. D. Pugh, C. Varadharajan, L. Zheng, M. Bianchi, P. S. Nico, N. F. Spycher, D. L. Newell, R. A. Esposito, Y. Wu, B. Dafflon, S. S. Hubbard and J. T. Birkholzer 2012. Effect of Dissolved CO2 on a Shallow Groundwater System: A Controlled Release Field Experiment. Environmental Science & Technology. In press.

Wang, S. and Jaffe, P. R., 2004. Dissolution of a mineral phase in potable aquifers due to CO_2 releases from deep formations; effect of dissolution kinetics. Energy Conversion and Management 45, 2833-2848.

Wilkin, R. T. and Digiulio, D. C., 2010. Geochemical impacts to groundwater from geologic carbon sequestration: controls on ph and inorganic carbon concentrations from reaction path and kinetic modeling. Environmental Science & Technology 44(12), 4821-4827.

Witter, A.E. and A.D. Jones, 1999. Chemical characterization of organic constituents from sulfide-rich produced water using gas chromatography/mass spectrometry. Environ. Toxicol. Chem., 18: 1920-1926.

Wolery, T. J., 1993. EQ3/6, A software package for geochemical modelling of aqueous systems (Version 7.2). , Lawrence Livermore National Laboratory. UCRL-MA 110662.

Xu, T., J.A. Apps, K. Pruess and H. Yamamoto, 2007. Numerical modeling of injection and mineral trapping of CO_2 with H_2S and SO_2 in a sandstone formation. Chemical Geology, 242: 319-346.

Xu, T., E. Sonnenthal, N. Spycher and K. Pruess, 2006. TOUGHREACT: a simulation program for non-isothermal multiphase reactive geochemical transport in variably saturated geologic media. Computers and Geosciences, 32: 145-165.

Zarrella, W.M., R.J. Mousseau, N.D. Coggeshall, M.S. Norris and G.J. Schrayer, 1967. Analysis and significance of hydrocarbons in subsurface brines. Geochem. Cosmochim. Acta, 31: 1155--1166.

Zheng, L., J.A. Apps, Y. Zhang, T. Xu and J.T. Birkholzer, 2009. On mobilization of lead and arsenic in groundwater in response to CO_2 leakage from deep geological storage. Chemical Geology, 268(3-4): 281-297.

Zheng, L., N. Spycher, Jens Birkholzer, T. Xu, J. Apps and Y. Kharaka 2010. Modeling studies on the transport of benzene and H2S in CO2-water systems, Lawrence Berkeley National Laboratory, technical report: LBNL-4339E.

Zheng, L., J. A. Apps, N. Spycher, J. T. Birkholzer, Y. K. Kharaka, J. Thordsen, S. R. Beers, W. N. Herkelrath, E. Kakouros and R. C. Trautz 2012. Geochemical modeling of changes in shallow groundwater chemistry observed during the MSU-ZERT CO2 injection experiment. International Journal of Greenhouse Gas Control 7(0): 202-217.

Caption of tables

Table 1. Hydrogeologic properties for the base model

Table 2. Hydrodynamic parameters.

Table 3. Initial total aqueous concentrations in the aquifer (pore water), computed by assuming initial equilibrium with aquifer minerals listed inTable B1.

Table 4. Mass distribution (mol% with respect to the total mass at t=0) of lead and arsenic on solid (in mineral or adsorbed on mineral surfaces) and liquid phase at initial time (t=0).

Table B1. Kinetic properties for minerals considered in the model (see text for data sources).

Table B2. Surface complexation of lead on different minerals.

Table B3. Surface complexation of arsenic on different minerals.

Captions of figures

Figure 1. Schematic representation of hypothetical 2-D simulation scenario.

Figure 2. Computed spatial distribution of SCC ("liquid") saturation after 3.5 years.

Figure 3. Spatial distribution of benzene mass fraction in the compressed "gas" phase at 1.5 years (a) and 3.5 years (b).

Figure 4. Spatial distribution of the concentration of aqueous benzene (molal) after 3.5 years

Figure 5. Computed solubilities of CO_2 and H_2S in water as a function of depth, following temperature gradient of 30°C/1000 m and hydrostatic pressure gradient.

Figure 6. Spatial distribution of the mass fraction of H_2S (a) and CO_2 (b) in the compressed "gas" plume after 3.5 years of injection.

Figure 7. Time evolution of the H_2S mass fraction (YH_2S) in the compressed "gas" plume at the bottom of the fracture (A), where the fracture connects to the storage formation, and at the top of the fracture (B), where the fracture connects to the overlying aquifer.

Figure 8. Schematic representation of the reactive transport modelsetup

Figure 9. Computed pH profile along x at y=0 at different times (the CO_2+H_2S mixture intrudes at x= 105 m). a) CO_2+H_2S leak, b)Pure CO_2 leak (from Zheng et al., 2009)

Figure 10. Predicted total aqueous sulfide concentration profile (as HS^-) along x at y=0 at different times (the CO_2+H_2S mixture intrudes at x= 105 m).

Figure 11. Profile of the pyrite volume fraction change (dimensionless) along x at y=0 at different times.

Figure 12. Computed profile of the goethite and siderite volume fraction change (dimensionless) along x at y=0 at 50 and 100 years.

Figure 13. Computed profile of lead concentration along x at y=0 at different time (the CO_2+H_2S mixture intrudes at x= 105 m). a) CO_2+H_2S leak, b)Pure CO_2 leak (from Zheng et al., 2009).

Figure 14. Computed profile of total sorbed arsenic concentrations along x at y=0 at different times.

Figure 15. Computed profile of total aqueous arsenic concentrations along x at y=0 at different times (the CO_2+H_2S mixture intrudes at x= 105 m). a) CO_2+H_2S leak, b)Pure CO_2 leak (from Zheng et al., 2009).

Figure 16. Computed profile of the arsenian pyrite and orpiment volume fraction change (dimensionless) along x at y=0 at different times.

Table 1. Hydrogeologic properties for the base model

Properties	**Values for deep storage formation, overlying aquifer**	**Values for aquitard**
Permeability (m^2)	1.0×10^{-13}	1.0×10^{-19}
Porosity	0.20	0.05
Capillary properties	Van Genuchten function with m=0.46, α =5.0×10^{-5}	Van Genuchten function with m=0.46, α =5.0×10^{-7}

Relative permeability	Corey's curve with zero residual gas saturation	Corey's curve with zero residual gas saturation
Residual water saturation	0.3	0.3

Table 2. Hydrodynamic parameters.

Porosity	0.3
Intrinsic permeability	1×10^{-12} m^2 (hydraulic conductivity of ≈ 0.86 m/day)
Relative permeability (van Genuchten-Mualem model)	$k_{rl} = \sqrt{S^*}\left\{1-\left(1-\left[S^*\right]^{1/0.457}\right)^{0.457}\right\}^2$ with $S^* = (S_l - 0.3)/(1.0-0.3)$ where S_l is the liquid saturation degree
Gas relative permeability	$k_{rg} = \left(1-\hat{S}\right)^2\left(1-\hat{S}^2\right)$ with $\hat{S} = \left(S_l - 0.3\right)/\left(1-0.3-0.05\right)$
Capillary pressure function	$P_{cap} = -\frac{1}{5.1\times10^{-5}}\left(\left[S^*\right]^{-1/0.457}-1\right)^{1-0.457}$ with $S^* = S_l/0.999$ and subject to restriction $-10^7 \le P_{cap} \le 0$
Molecular diffusion coefficient	10^{-9} m^2/s
Tortuosity	0.3

Table 3. Initial total aqueous concentrations in the aquifer (pore water), computed by assuming initial equilibrium with aquifer minerals listed inTable B1.

Species	Concentration (mol/L)	Species	Concentration (mol/L)
Ca	9×10^{-4}	TIC	3.3×10^{-3}
Mg	2.2×10^{-5}	SO_4^{-2}	1.9×10^{-4}
Na	2×10^{-3}	Cl	2.1×10^{-4}
K	2.7×10^{-4}	Pb	1.3×10^{-9}
Fe	5.6×10^{-6}	As	4.4×10^{-8}
HS^-	$1.4\times\times10^{-8}$	HSe^-	1.7×10^{-9}
Si	9.3×10^{-4}	Eh	-0.23 V
pH	7.6	ionic strength	0.0051

Table 4. Mass distribution (mol% with respect to the total mass at t=0) of lead and arsenic on solid (in mineral or adsorbed on mineral surfaces) and liquid phase at initial time (t=0).

	Aqueous Phase (%)	Mineral (%)	Adsorbed on goethite (%)	Adsorbed on kaolinite (%)	Adsorbed on illite (%)	Adsorbed on smectite (%)	Total Adsorbed (%)	Total in sediments (ppm)
Lead	0.003	99.89	0.01	0.002	0.04	0.0003	0.05	10.01
Arsenic	0.01	36.80	8.49	4.54	38.26	11.90	63.19	28.39

Table B1. Kinetic properties for minerals considered in the model (see text for data sources).

Mineral	A (cm^2/g)	Parameters for Kinetic Rate Law							
		Neutral Mechanism		Acid Mechanism			Base Mechanism		
		k_{25} ($mol/m^2/s$)	E_a (KJ /mol)	k_{25}	E_a	$n(H^+)$	k_{25}	E_a	$n(H^+)$
***Primary*:**									
Quartz	9.8	1.023×10^{-14}	87.7						
K-feldspar	9.8	3.89×10^{-13}	38	8.71×10^{-11}	51.7	0.5	6.31×10^{-12}	94.1	-0.823
Oligoclase	9.8	1.44×10^{-12}	69.8	2.13×10^{-10}	65	0.457			
Kaolinite	151.6	6.91×10^{-14}	22.2	4.89×10^{-12}	65.9	0.777	8.91×10^{-18}	17.9	-0.472
Smectite-Ca	151.6	1.66×10^{-13}	35	1.05×10^{-11}	23.6	0.34	3.02×10^{-17}	58.9	-0.4
Illite	151.6	1.66×10^{-13}	35	1.05×10^{-11}	23.6	0.34	3.02×10^{-17}	58.9	-0.4
Chlorite	9.8	3.02×10^{-13}	88	7.76×10^{-12}	88	0.5			
Kerogen-os	9.8	3.02×10^{-13}	88	7.76×10^{-12}	88	0.5			
Calcite	Assumed at equilibrium								
Goethite	12.9	2.52×10^{-12}	62.76						
Arsenian pyrite	12.9	2.52×10^{-12}	62.76						
Pyrite	12.9	2.52×10^{-12}	62.76						
Galena	12.9			2.34×10^{-7}	43.54	1			
Secondary:									
Dolomite	12.9	2.52×10^{-12}	62.76	2.34×10^{-7}	43.54	1			
Magnesite	9.8	4.57×10^{-10}	23.5	4.17×10^{-7}	14.4	1			
Ankerite	9.8	1.26×10^{-9}	62.76	6.46×10^{-4}	36.1	0.5			
Dawsonite	9.8	1.26×10^{-9}	62.76	6.46×10^{-4}	36.1	0.5			
Smectite-Na	151.6	1.66×10^{-13}	35	1.05×10^{-11}	23.6	0.34	3.02×10^{-17}	58.9	-0.4
Pyromorphite	12.9	2.52×10^{-12}	62.76	2.34×10^{-7}	43.54	1			
Ferroselite	12.9	2.52×10^{-12}	62.76	2.34×10^{-7}	43.54	1			
Orpiment	12.9	2.52×10^{-12}	62.76	2.34×10^{-7}	43.54	1			
Realgar	12.9	2.52×10^{-12}	62.76	2.34×10^{-7}	43.54	1			
siderite	9.8	1.26×10^{-9}	62.76	6.46×10^{-4}	36.1	0.5			

Table B2. Surface complexation of lead on different minerals.

Adsorbent	Surface Complexes	Reactions	Log k_{int}	Reference
Goethite	Goe_OPb^+	$Goe\_OPb^+ + H^+ = Goe\_OH + Pb^{+2}$	0.5	(Muller and Sigg, 1991)
Goethite	$(Goe\_O)_2Pb$	$(Goe\_O)_2Pb+2H^+ = 2Goe\_OH + Pb^{+2}$	6.24	
kaolinite	Kao_OPb^+	$Kao\_OPb^+ + H^+ = Kao\_OH + Pb^{+2}$	-1.89	(Hizal and Apak, 2006)
Illite	$Ill^s\_OPb^+$	$Ill^s\_OPb^+ + H^+ = Ill^s\_OH + Pb^{+2}$	-1.37	(Gu and Evans, 2007)
Illite	$Ill^w\_OPb^+$	$Ill^w\_OPb^+ + H^+ = Ill^w\_OH + Pb^{+2}$	3.84	
smectite	$Sme^s\_OPb^+$	$Sme^s\_OPb^+ + H^+ = Sme^s\_OH + Pb^{+2}$	-1.12	(Bradbury and Baeyens, 2005)
smectite	$Sme^w\_OPb^+$	$Sme^w\_OPb^+ + H^+ = Sme^w\_OH + Pb^{+2}$	1.28	

Table B3. Surface complexation of arsenic on different minerals.

Adsorbent	Surface Complexes	Reactions	Log k_{int}	Reference
Goethite	Goe _H_2AsO_3	Goe _H_2AsO_3 + H_2O = Goe _OH + H_3AsO_3	-5.19	(Dixit and Hering, 2003)
goethite	Goe _$HAsO_3^-$	Goe _$HAsO_3^-$ + H_2O + H^+ = Goe_OH + H_3AsO_3	2.34	
kaolinite	Kao_H_2AsO_3	Kao _H_2AsO_3 + H_2O = Kao _OH + H_3AsO_3	-8.23	(Manning and Goldberg, 1997)
kaolinite	Kao _$HAsO_3^-$	Kao_$HAsO_3^-$ + H_2O + H = Kao _OH + H_3AsO_3	0.664	
kaolinite	Kao _$OAsO_3^{2-}$	Kao_AsO_3^{2-} + H_2O + $2H^+$ = Kao _OH + H_3AsO_3	13.67	
illite	Ill_H_2AsO_3	Ill _H_2AsO_3 + H_2O = Ill_OH + H_3AsO_3	-9.07	(Manning and Goldberg, 1997)
illite	Ill _$HAsO_3^-$	Ill _$HAsO_3^-$ + H_2O + H^+ = Ill _OH + H_3AsO_3	-3.0	
illite	Ill_AsO_3^{2-}	Ill_AsO_3^{2-} + H_2O + $2H^+$ = Ill_OH + H_3AsO_3	10.3	
smectite	Sme _H_2AsO_3	Sme _H_2AsO_3 + H_2O = Sme _OH + H_3AsO_3	-8.89	(Manning and Goldberg, 1997)
smectite	Sme _$HAsO_3^-$	Sme _$HAsO_3^-$ + H_2O + H^+ = Sme _OH + H_3AsO_3	4.65	
smectite	Sme _AsO_3^{2-}	Sme _AsO_3^{2-} + H_2O + $2H^+$ = Sme _OH + H_3AsO_3	13.7	

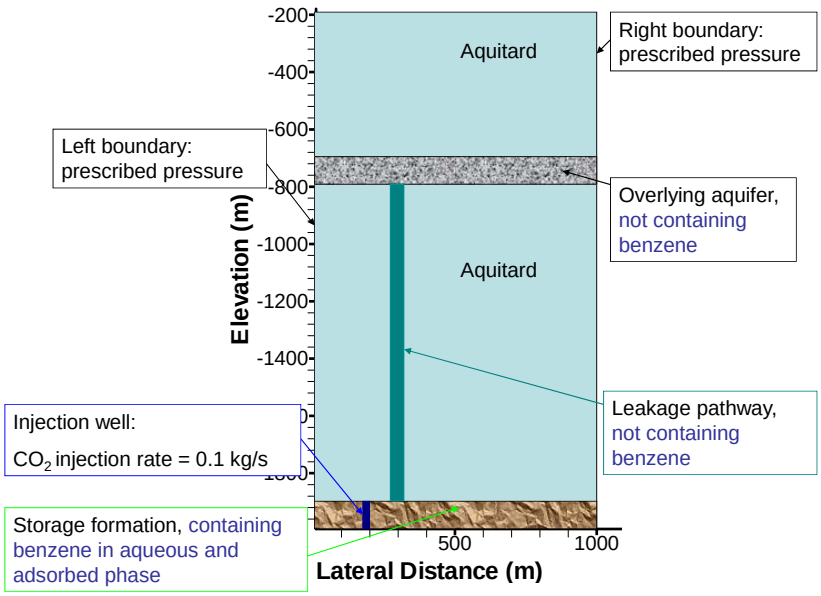

Figure 1. Schematic representation of hypothetical 2-D simulation scenario.

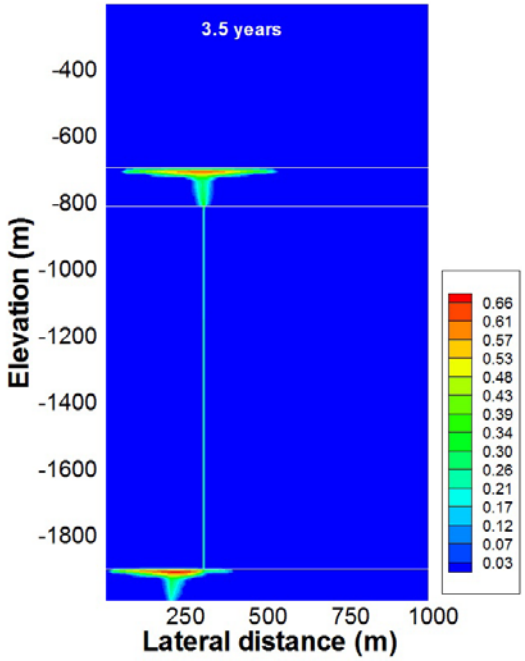

Figure 2. Computed spatial distribution of SCC ("liquid") saturation after 3.5 years.

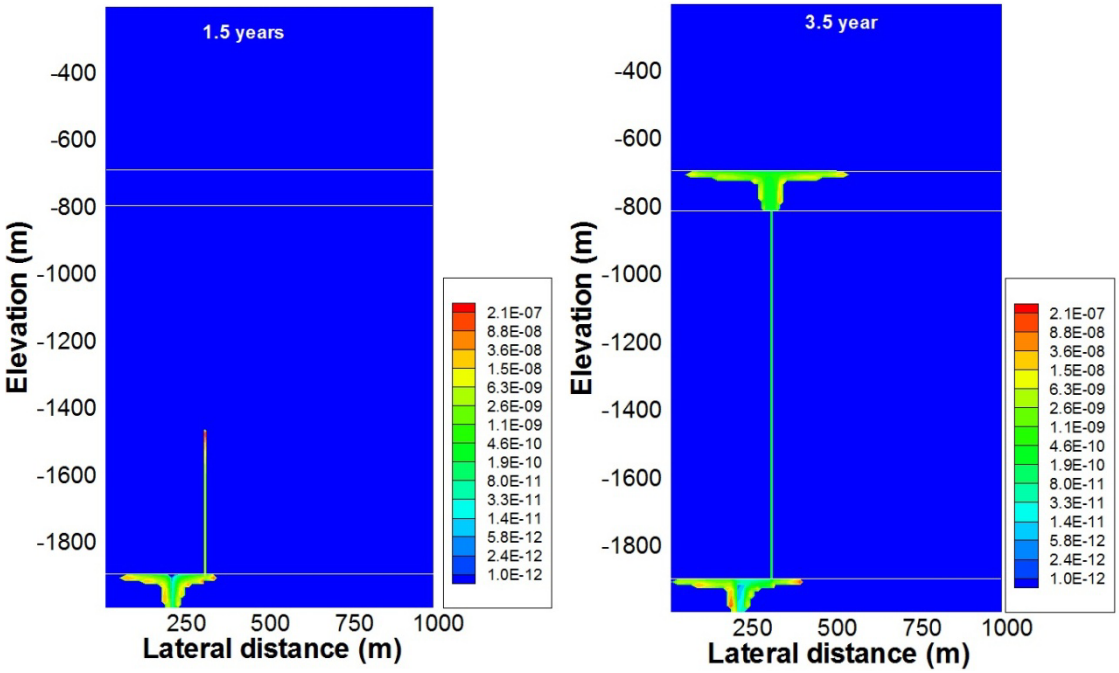

(a) (b)

Figure 3. Spatial distribution of benzene mass fraction in the compressed "gas" phase at 1.5 years (a) and 3.5 years (b).

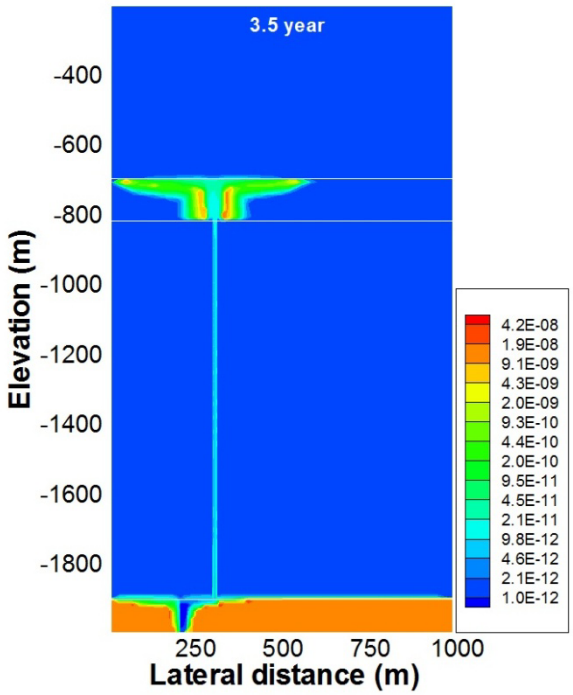

Figure 4. Spatial distribution of the concentration of aqueous benzene (molal) after 3.5 years

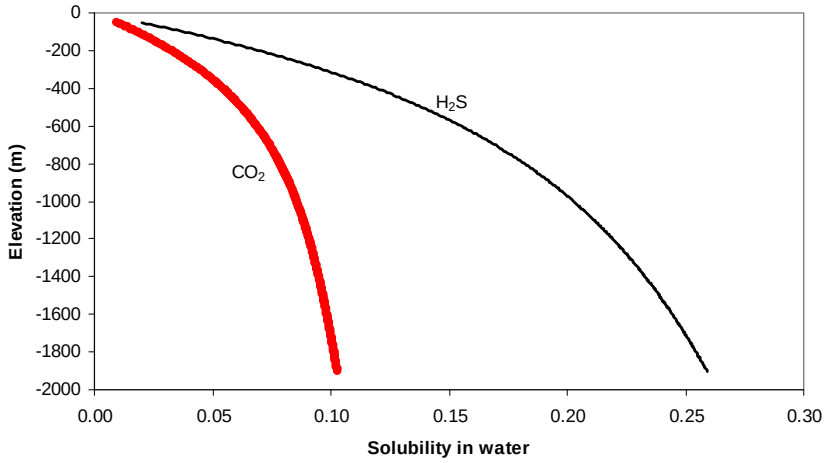

Figure 5. Computed solubilities of CO_2 and H_2S in water as a function of depth, following temperature gradient of 30°C/1000 m and hydrostatic pressure gradient.

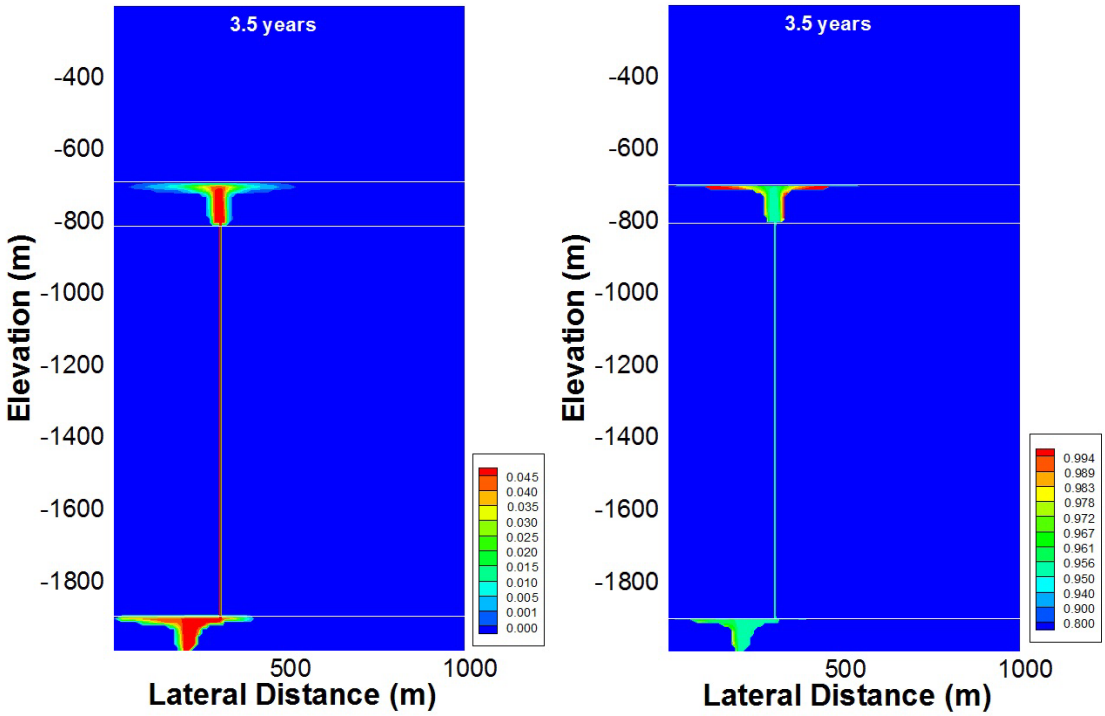

(a) (b)

Figure 6. Spatial distribution of the mass fraction of H_2S (a) and CO_2 (b) in the compressed "gas" plume after 3.5 years of injection.

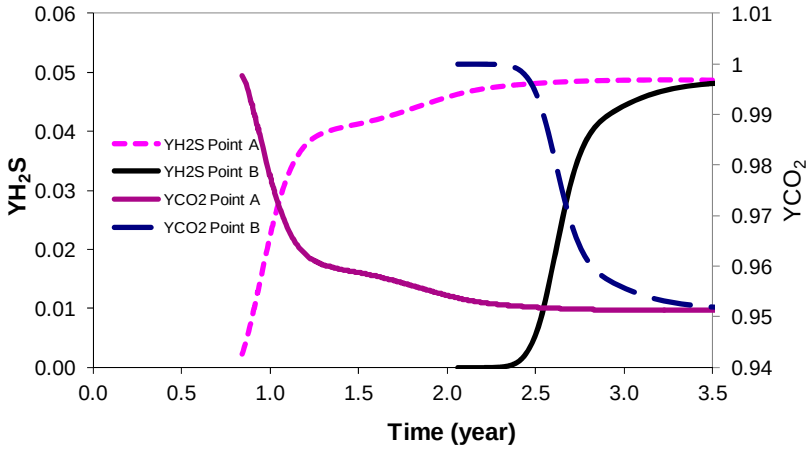

Figure 7. Time evolution of the H_2S mass fraction (YH_2S) in the compressed "gas" plume at the bottom of the fracture (A), where the fracture connects to the storage formation, and at the top of the fracture (B), where the fracture connects to the overlying aquifer.

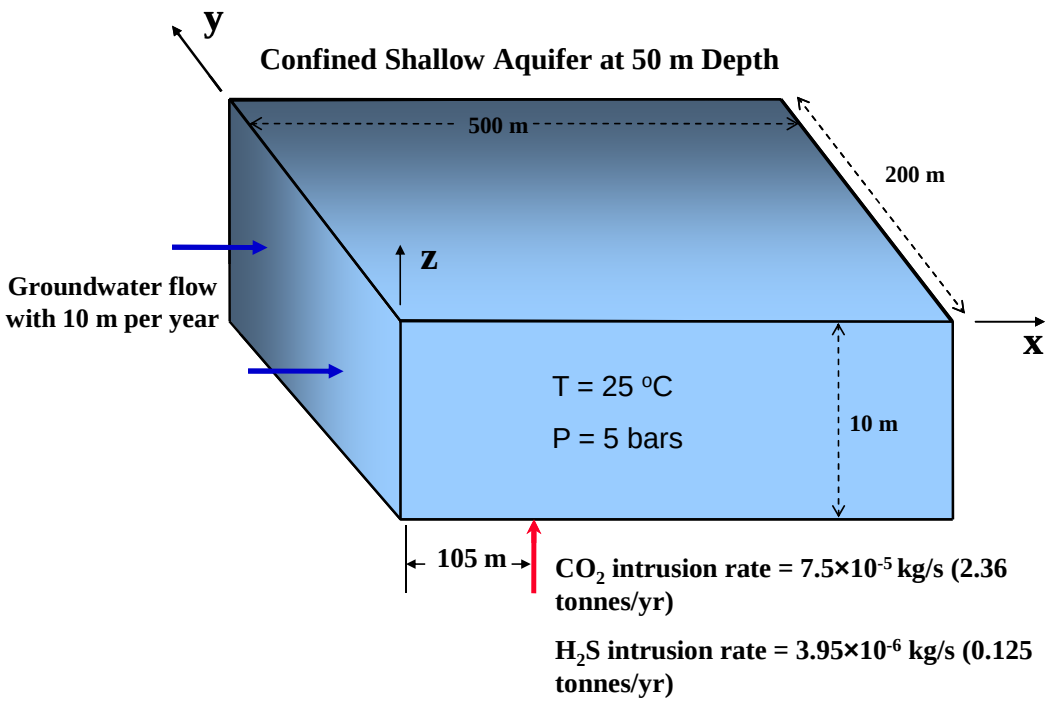

Figure 8. Schematic representation of the reactive transport modelsetup

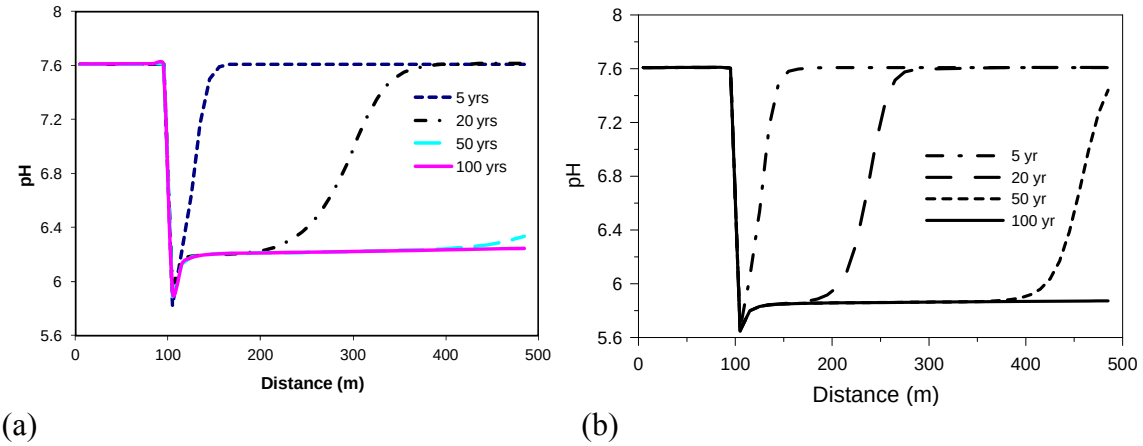

Figure 9. Computed pH profile along x at y=0 at different times (the CO_2+H_2S mixture intrudes at x= 105 m). a) CO_2+H_2S leak, b)Pure CO_2 leak (from Zheng et al., 2009)

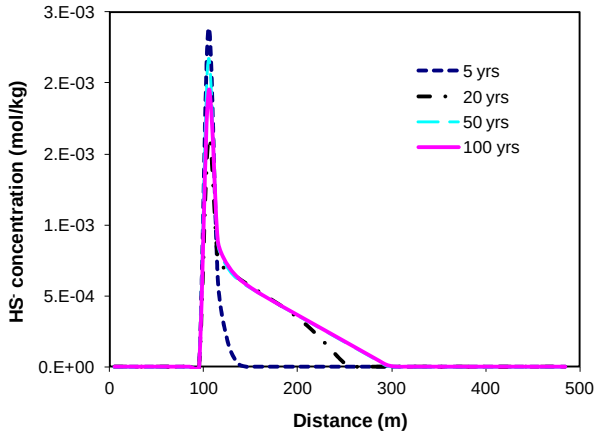

Figure 10. Predicted total aqueous sulfide concentration profile (as HS^-) along x at y=0 at different times (the CO_2+H_2S mixture intrudes at x= 105 m).

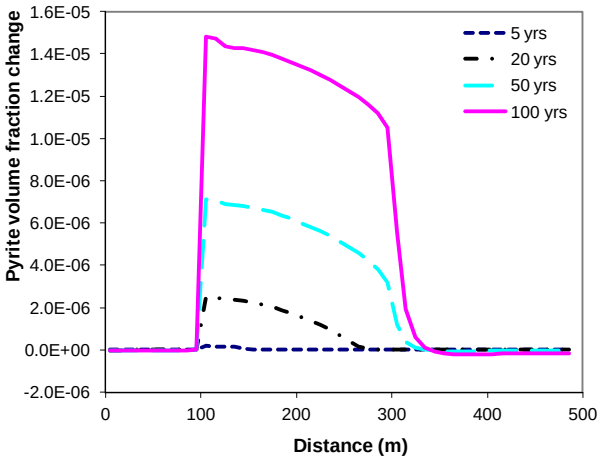

Figure 11. Profile of the pyrite volume fraction change (dimensionless) along x at y=0 at different times.

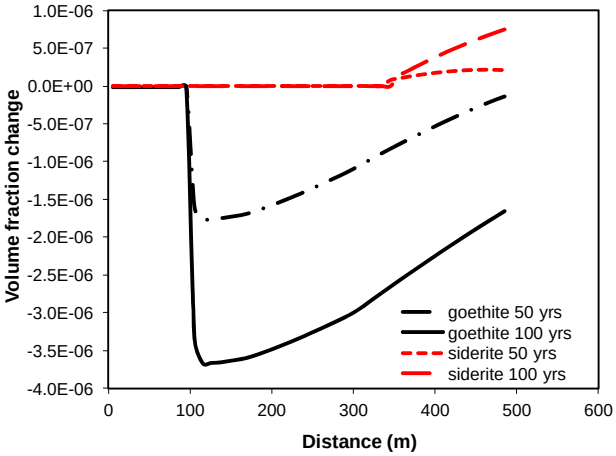

Figure 12. Computed profile of the goethite and siderite volume fraction change (dimensionless) along x at y=0 at 50 and 100 years.

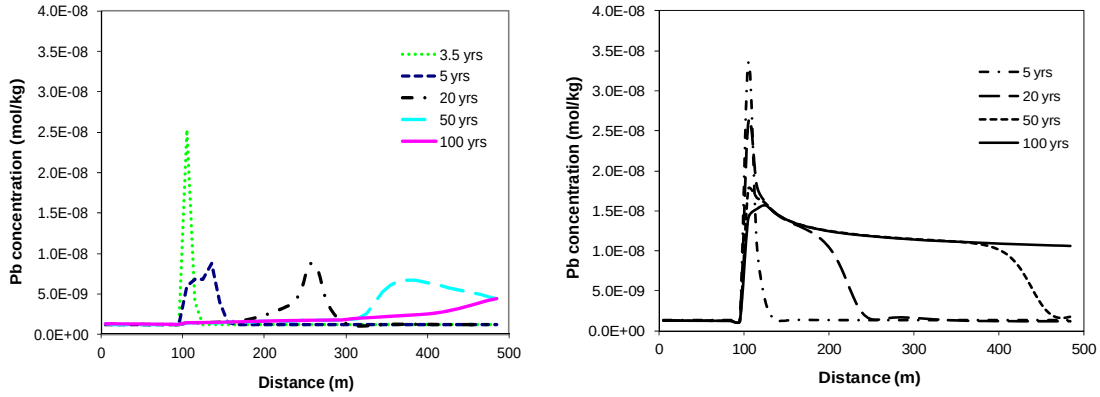

(a) (b)

Figure 13. Computed profile of lead concentration along x at y=0 at different time (the CO_2+H_2S mixture intrudes at x= 105 m). a) CO_2+H_2S leak, b)Pure CO_2 leak (from Zheng et al., 2009).

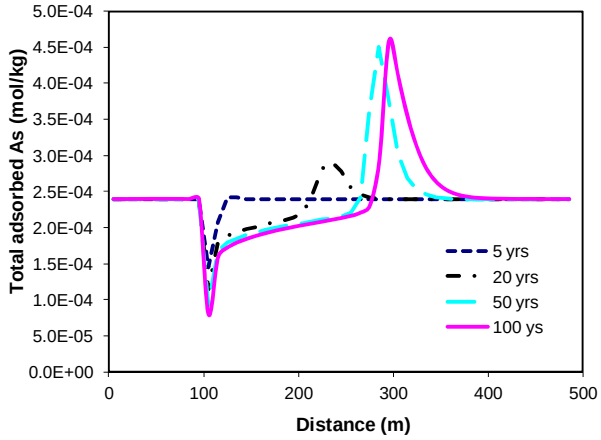

Figure 14. Computed profile of total sorbed arsenic concentrations along x at y=0 at different times.

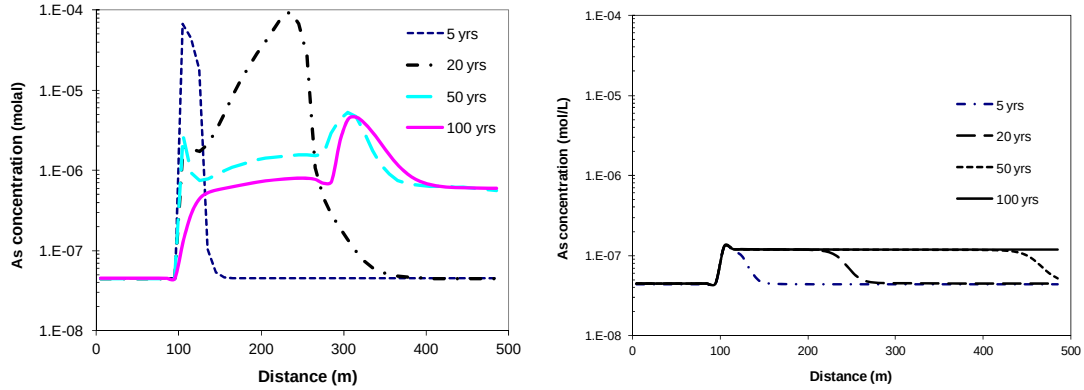

(a) (b)

Figure 15. Computed profile of total aqueous arsenic concentrations along x at y=0 at different times (the CO_2+H_2S mixture intrudes at x= 105 m). a) CO_2+H_2S leak, b)Pure CO_2 leak (from Zheng et al., 2009).

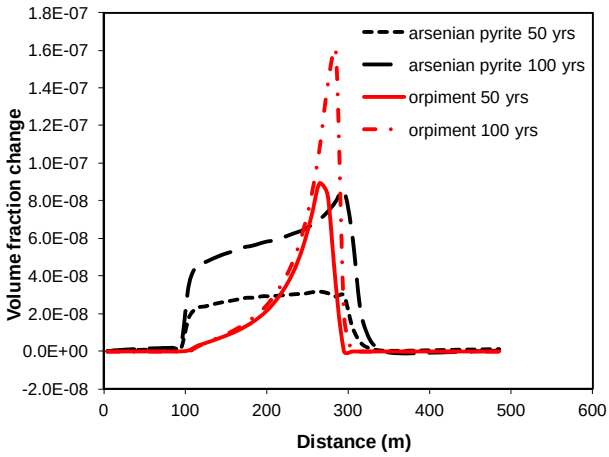

Figure 16. Computed profile of the arsenian pyrite and orpiment volume fraction change (dimensionless) along x at y=0 at different times.